Chapter 6

Ion beam led modification of PPy-MoS_2 nanocomposites for highly sensitive immunosensor application

---

Earlier chapters have described the fabrication of enzymatic and non-enzymatic sensors for detection of diferent target analytes. In every work, the transducers were designed in such a way that they could offer better signal amplification, higher sensitivity, enhanced catalytic activity with good electrochemical performance. Based upon the requirements and material performance, we have utilized conducting polymer and 2D layered material based composite systems to work as transduction element. To be mentioned, the physico-chemical and other spectroscopic properties of theses composite systems can be further improved by performing ion beam mediated modifications. The highly energetic ions can potentially control the electrochemical performance of the transducer depending upon the fluence used. In the current chapter, the effect of energetic ion beams on the sensing performance of a conducting polymer-based immunosensor probe is studied with care. Here, our aim is to perform a comparative assessment on the fluence dependent material modifications and its potential application as electrochemical immunosensor.

6.1.Introduction

As mentioned in the Chapter 1, the transducer plays a major role in the electrochemical biosensors towards improving the detection mechanism and parameters there in. To further enhance the performance of the immunosensor, surface modification of the transducer is very crucial. As highlighted in section 1.4 of Chapter 1, SHI is an effective technique that can reshape different properties of the target material in a much controlled manner. In this method, a highly energetic ion beam is bombarded on the sample that causes excitation and ionization in the electronic sub-system of the target atoms. Ion-matter interaction is inelastic in case of SHI irradiation and the electronic energy loss ($(dE/dx)_e$) dominates the energy transfer mechanism. The inhomogeneous energy transfer occurring through electron-phonon coupling

eventually drives the formation of amorphous tracks in the SHI irradiated specimen [218]. Morphological modification, changes in physico-chemical and spectroscopic behaviour are some of the vital aspects expected after SHI irradiation.

In this work, a hybrid nanocomposite of polypyrrole and MoS_2 was synthesized by simple hydrothermal route and irradiated with 90 MeV C^{6+} ion beams (fluence ranging from 1.0×10^{10} to 1.0×10^{13} ions/cm^2). Being a conducting polymer, polypyrrole exhibits good conductivity, electrochemical activity, less toxicity and water stability. The functional fragments present in the polymer chain also gives advantage for better immobilization of biomolecules through covalent linkage. It has been reported that the conductivity as well as the electrochemical performance of polypyrrole can be enhanced significantly via high energy ion beam irradiation technique [219, 220]. Moreover, MoS_2 is a potential candidate in the field of electrochemical sensing which has already been highlighted in section 3.1 and section 1.4. This inspired us to prepare a PPy-MoS_2 nanocomposite-based transducer material for fabrication of electrochemical sensor. Also, the effect of energetic ion beam on the performance of the electrochemical immunosensor is discussed in detail.

6.2 Experimental

6.2.1. Synthesis of Polypyrrole (PPy)

2 mM Pyrrole solution was prepared in 70 mL dilute HCl containing water and acid in 9:1 ratio. Also, 25 mL of 0.5 M ammonium persulfate (APS) solution was separately prepared in DI water. Above two solutions were mixed in a beaker and stirred (~ 400 rpm) vigorously for 3 h. Then, the solution was transferred to a 100 mL teflon lined stainless steel autoclave and kept at a temperature of 180^{o}C for 24 h. After completion of the hydrothermal reaction, the mixture was cooled down to room temperature followed by washing the precipitate with ethanol and water. Finally, the black PPy powder was collected by drying the precipitate overnight at a temperature of 60^{o}C [221].

6.2.2. Synthesis of layered MoS_2

The synthesis procedure for layered MoS_2 has already been described in section 5.2.1 of Chapter 5.

6.2.3. Synthesis of PPy-MoS_2

2 mM Pyrrole solution was prepared in 70 mL dilute HCl containing 4 mL of 1.5 mg/mL aqueous MoS_2 suspension. Again, 0.5 M APS solution was separately prepared in 25 mL DI

water. The above two solutions were mixed in a beaker and stirred vigorously for 3 h. Then the solution was transferred into a 100 mL stainless steel autoclave and heated at a temperature of 180^oC for 24 h. The mixture was naturally cooled down to room temperature after the hydrothermal treatment and followed by washing the precipitate with ethanol and water. Lastly, the PPy-MoS_2 nanocomposite powder was yielded by oven drying the precipitate overnight at a temperature of 60^oC.

6.2.4. Preparation of PPy-MoS_2 deposited electrode

3 mg of the as prepared PPy-MoS_2 NPs was taken along with 5 wt% of poly-vinylidene fluoride (PVDF) used as binder. The binder and the electroactive specimen (PPy-MoS_2) were dispersed in 50µL of N-Methyl-2-Pyrrolidone (NMP). They were mixed properly in the form of slurry and casted over the 0.5 cm^2 area of the Indium Tin Oxide (ITO) electrodes. Then, they were dried overnight at a temperature of 60^oC in a hot air oven to obtain the PPy-MoS_2 deposited ITO electrode.

6.2.5. Preparation of PPy-MoS_2 pellet

Firstly, teflon pellets of 1.3 cm diameter were prepared by hard-pressing the commercially available teflon tape on hydraulic press at 60 bar pressure. Afterwards, PPy-MoS_2 powder was sprinkled uniformly over the surface of the teflon pellet and again pressed in the hydraulic press (at 50 bar pressure) to obtain the Teflon supported PPy-MoS_2 covered pellets.

6.2.6. SHI irradiation on the PPy-MoS_2 nanocomposite

Both PPy-MoS_2 covered pellets and PPy-MoS_2 deposited ITO electrodes were loaded inside the ion irradiation chamber where 90 MeV C^{6+} ions were allowed to irradiate on our specimens. Four fluences *viz*. 1.0×10^{10}, 3.5×10^{11}, 1.0×10^{12} and 1.0×10^{13} ions/cm^2 were chosen for observing irradiation led modification in our samples. To be mentioned, the thickness of the samples (pellets and films) that we had prepared are of ~100 µm and our motivation was to pass the ion beam through the specimen. Simulation through SRIM software® reveals that 90 MeV carbon beam will be suitable for our experiment which can offer a projectile range of 132 µm and an electronic stopping (dE/dx) value of 1.379 keV/(µg.cm^{-2}). Also, the fluence variation was kept in the range of 10^{10} to 10^{13} ions/cm^2.

6.2.7. Fabrication of the immunosensor

Immobilization of mouse *IgG* (antibody) over the PPy-MoS_2 deposited electrode was performed via glutaraldehyde cross-linking method by following the procedure as described in section 2.2.5 of Chapter 2.

6.3 Results and discussion

6.3.1. X-ray diffraction (XRD) and infrared spectroscopy (FT-IR) study

The XRD responses of the as synthesized MoS_2, PPy and PPy-MoS_2 systems are depicted in Figure 6.1(a). The characteristic diffraction peak of MoS_2 appeared at 2θ = 14.5° and corresponds the (002) crystallographic plane. Other significant peaks appearing at 34.6°, 39.3° and 58.7° resemble (011), (013) and (112) planes of MoS_2 respectively. In the diffraction response for PPy, a broad peak appearing at 2θ~26° is ascribed to the π-π interaction in the PPy chains, indicating semi crystalline nature of the polymer system [222]. Whereas, the appearance of PPy and MoS_2 peaks in the uppermost diffractogram indicate the presence of both polymer and TMDC constituents in the composite system. On the other hand, all the vibrational bands of PPy can be observed in the FT-IR spectrum of Figure 6.1(b). However, the strength of the IR bands tending to drop in case of PPy-MoS_2 spectrum due to the formation of the nanocomposite system.

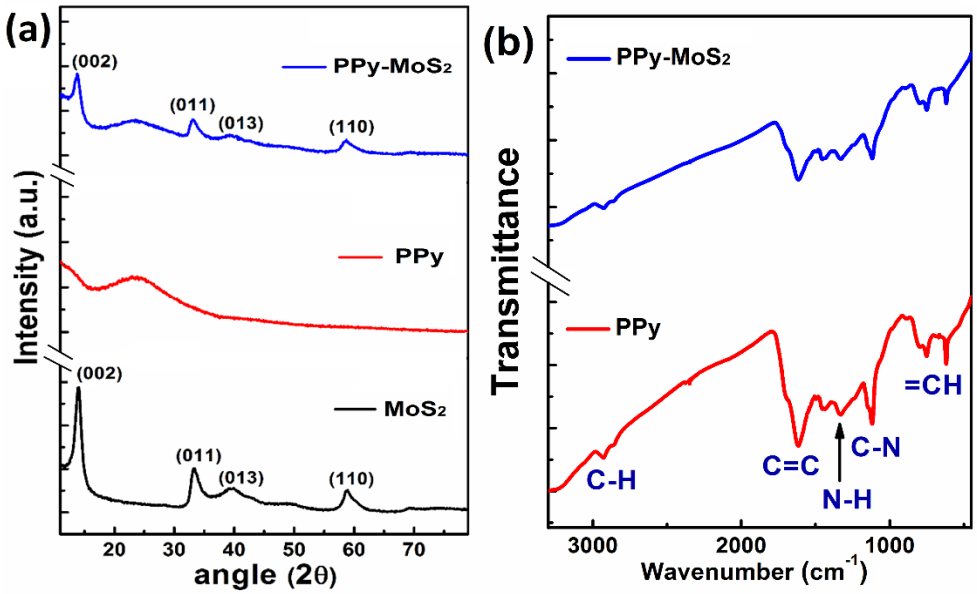

Figure 6.1: (a) XRD patterns of MoS_2, PPy and PPy-MoS_2, and (b) FT-IR characteristics of PPy and PPy-MoS_2 systems

The XRD patterns of the pristine and irradiated PPy-MoS_2 composite systems are depicted in Figure 6.2(a). As for XRD characterization, teflon supported PPy-MoS_2 pellets (see section 6.2.5) were used directly without removing or scratching off. The violet curve represents the XRD response of the blank teflon (being used as support material), which offers a sharp characteristic peak at the diffraction angle, $2\theta \sim 18.7^o$ [223]. Due to the presence of teflon at the base of each sample, this sharp characteristic peak will appear in all the spectra which eventually dominates the intensity of other less prominent peaks. To avoid this, the sharp teflon peak was omitted from the plots by breaking the data points in between 15.0^o-20.0^o. The 2^{nd} spectrum of Figure 6.2(a) represents the XRD response of the PPy-MoS_2 composite system where sharp diffraction peak appeared at, $2\theta = 12.5^o$ and a less prominent peak at, $2\theta = 34.6^o$. At the lowest fluence of 1.0×10^{10} ions/cm^2, the characteristic peaks of the composite system have disappeared due to the breaking of the polymer backbones, and creation of the amorphous tracks throughout the path of the energetic C^{6+} ions. These peaks again reappeared may be due to the recrystallization, and became prominent at the fluence of 3.5×10^{11} ions/cm^2 and higher. This is because of the fact that on increasing the ion fluence, cross-linking occurs in the polymer matrix that results in the reordering and restacking of the polymer chains. In the XRD responses, the peaks become less prominent and almost disappeared at the highest fluence of 1.0×10^{13} ions/cm^2. This can be ascribed to the massive overlapping of the irradiated tracks which could degrade the crystallinity of the composite system eventually.

The FT-IR responses of the pristine and irradiated PPy-MoS_2 composite systems are shown in Figure 6.2(b). First, the samples are collected by peeling off the irradiated specimen from the teflon pellet and then processed for FT-IR study. The black spectrum illustrates the FT-IR response of the pristine PPy-MoS_2 composite system. In this spectrum, the characteristic vibrational bands appear at ~ 1628 cm^{-1} and 1123 cm^{-1} corresponding to the C=C and C-N bonding of the pyrrole ring, respectively. The small IR bands emerging ~ 2929 cm^{-1} resembles the C-H bond vibration followed by a significant N-H vibrational mode at 1325 cm^{-1}. In addition, the vibrational peak appearing in the spectrum at ~ 765 cm^{-1} represents the out of plane vibration of =CH group [100]. The Mo-S vibrational band generally appears at ~ 450 cm^{-1} which could got suppressed in our case due to the development of the composite system. In this regard, the intensity of the vibrational bands of PPy drops significantly after incorporation of the MoS_2 in the polymer matrix (Figure 6.1(b)), indicating that the functional

groups in the polymer grains have experienced constraints against their relaxation due to the insertion of MoS_2 sheets in the polymer matrix. In Figure 6.2(b), a noticeable change in the vibrational band intensity has been found in the composite system upon treatment with different ion doses due to the consequence of SHI impact. Upon increasing the ion fluence, an anomalous breaking and formation of different inter/intra-atomic bonds can be realized from the vibrational band intensity of the IR spectra. The excess breaking of the polymer chains at the highest fluence of 1.0×10^{13} ions/cm^2 generates a large extent of freely oscillating functional groups that give rise to the most prominent absorption peaks in the corresponding IR spectrum, within the range of 1000-1800 cm^{-1}. On the other hand, less intense vibrational bands can be seen at a moderate fluence of 3.5×10^{11} ions/cm^2, suggesting cross-linking of the polymer chains occurring at this moderate fluence. The absorption peak positioned at 765 cm^{-1} attributed to the out of plane vibration of =CH bond and a considerable augmentation in intensity can be observed at the highest fluence. The evolution of this peak at the maximum fluence might be due to the creation of freely dangled =CH group at the edge of the polymer backbones being generated via excessive chain scissioning.

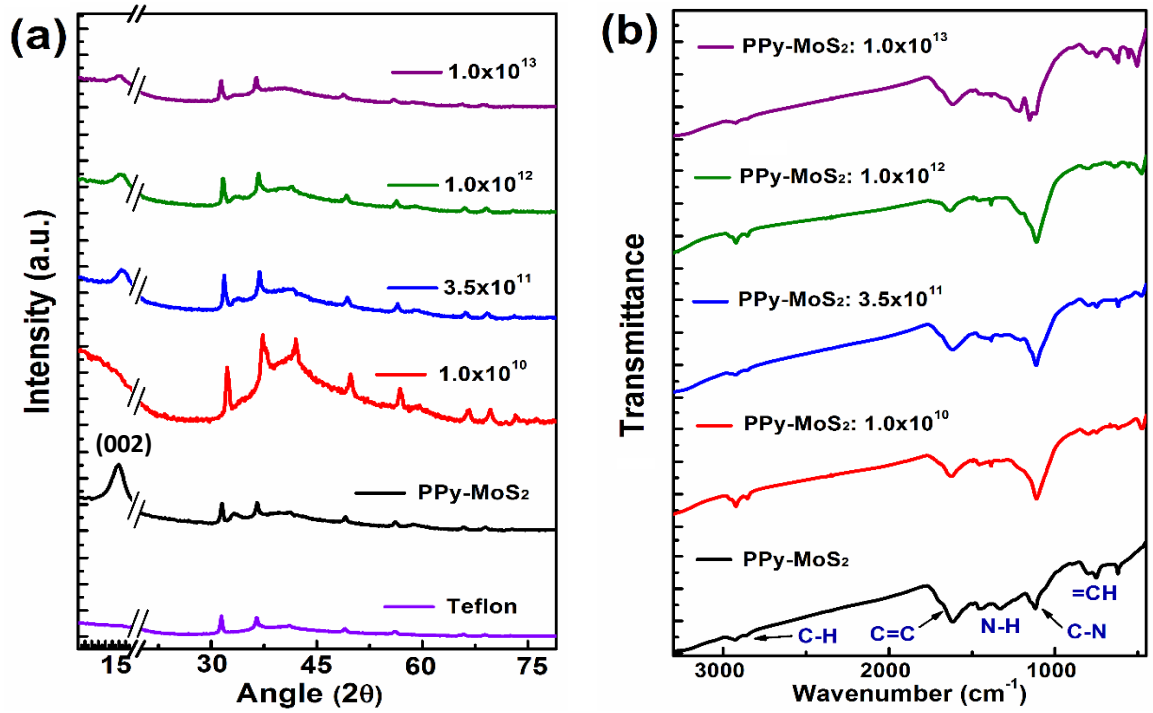

Figure 6.2: (a) XRD and (b) FT-IR, responses of the pristine system and irradiated systems with fluence 1.0×10^{10}, 3.5×10^{11}, 1.0×10^{12} and 1.0×10^{13}, ions/cm^2

To further realize the anomalous shifting and vanishing of the diffraction peaks, a magnified view of the XRD spectra corresponding to the (002) crystallographic plane of the pristine and irradiated systems has been plotted in Figure 6.3. The layered stacking of MoS_2 sheets along (002) crystallographic direction gives rise to the sharp peak at 2θ =14.5°. This peak got suppressed when exposed to 90 MeV carbon ion irradiation at a fluence of 1.0×10^{10} ions/cm^2, indicating an increase in the degree of disorderness amongst the MoS_2 sheets. The random stacking of MoS_2 in the composite system might have occurred due to the disordered chain scissioning taking place in the polymer matrix at 1.0×10^{10} ions/cm^2 fluence [224]. Again, the (002) diffraction peak shifted towards a higher Bragg's angle position (at 3.5×10^{11} ions/cm^2 fluence) due to a decrease in the interplanner spacing of MoS_2 layers. At this flux rate, the cross-linked polymer chains might have assisted the contraction of the MoS_2 layers in the composite system causing homogeneous dispersion between MoS_2 and the polymer matrix with improved interfacial contact [102]. In Figure 6.3, it is also noticeable that the (002) diffraction peak starts to move towards a lower Bragg's angle position on increasing fluence, which in fact indicates a rise in the interlayer gap of the MoS_2 layers. This might occur due to the defects produced *via* excessive heat deposition leading to disordered chain breaking followed by poor dispersion of MoS_2 in the polymer backbone. Furthermore, the decrease in peak height upon increasing fluence signifies adequate exfoliation of incorporated MoS_2 sheets driven by ion-matter interaction.

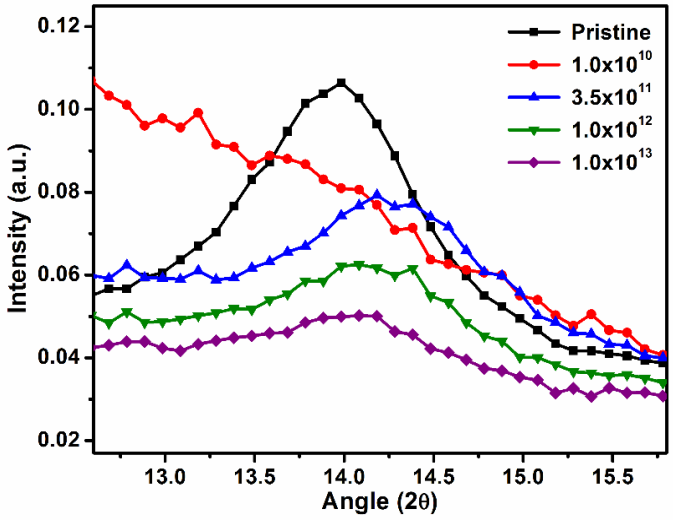

Figure 6.3: Magnified diffraction pattern of the (002) peak of pristine and irradiated PPy-MoS_2 system

6.3.2. Field emission scanning electron microcopy (FESEM) study

Electrochemical behaviour of an electrode largely depends on its surface morphology. Generally, porous nanostructures having uniform particle distribution are beneficial for good electrolytic contact. Also, a better composite architecture of different nano units can improve the carrier transportation and modulate the electrocatalytic activity of the nanosystem. The surface morphology of the pristine and irradiated PPy-MoS_2 systems were visualized from the FESEM images captured at different magnifications (Figure 6.4). The uniform growth of the polypyrrole grains over the MoS_2 sheet and the distribution of the fine polymer units can be viewed Figure 6.4(a.1) and in the magnified image of Figure 6.4(a.2). As can be found in Figure 6.4(b), at the moderate fluence of 3.5×10^{11} ions/cm^2, carbon ion irradiation (90 MeV) would impart substantial damage to the target material. In Figure 6.4(b.1), the irregular breaking of the large MoS_2 sheets along with the wide distribution of interconnected polymer nanograins confirm the ion beam mediated modification of the PPy-MoS_2 composite system. Here, the energy transfer mechanism has stripped apart the agglomerated polymer units to form large amount of cross-linked polymer nanostructure which ultimately improve the carrier transport. Such distribution of polymer nanograin can enrich the effective surface contact of the system providing superior electrocatalytic activity. Also, these energetic C^{6+} ions are strong enough to break as well as move apart the MoS_2 sheets resulting in the formation of small MoS_2 flakes, as can be viewed in Figure 6.4(b.2). The FESEM micrograph of the system irradiated with the highest fluence of 1.0×10^{13} ions/cm^2 illustrates the damage caused by the energetic C^{6+} ions over to the PPy-MoS_2 composite surface, as evident from Figure 6.4(c.1, c.2). During high fluence, the target lattice has to go through enormous thermal annealing induced by the energy transfer via electron-phonon coupling. This eventually leads to permanent structural as well as morphological modification of the target. In Figure 6.4(c.1), we can observe the formation of large aggregated polymer grains after irradiating the target with the highest fluence. The small nanopores which can be observed in the magnified image are basically the ion tracks that are generated throughout the trajectory of the energetic C^{6+} ions.

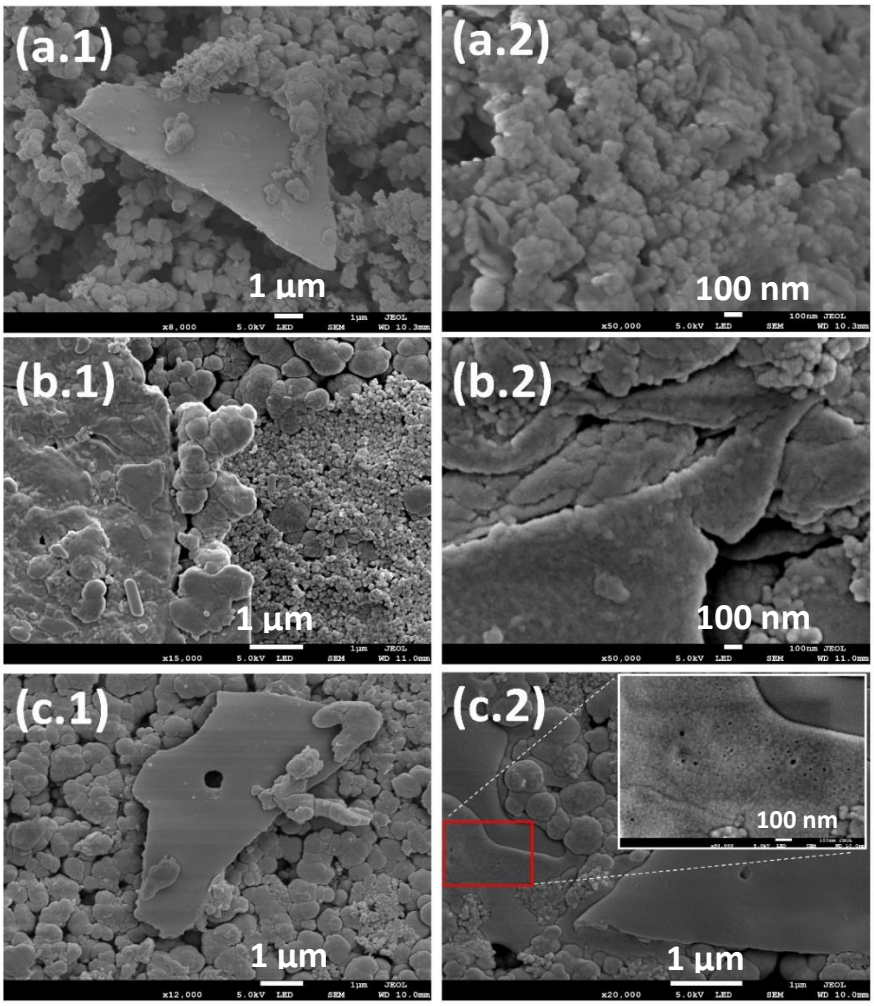

Figure 6.4: FESEM micrograph of (a.1, a.2) PPy-MoS_2 (pristine), and irradiated PPy-MoS_2 nanocomposites when subjected to fluences of (b.1, b.2) 3.5×10^{11} ions/cm^2, (c.1, c.2) 1.0×10^{13} ions/cm^2 at different magnifications

6.3.3. Transmission electron microscopy (TEM) analysis

From the TEM micrographs shown in Figure 6.5(a.1) and (a.2), the polypyrrole nanograins are seemed to be dispersed under the MoS_2 sheets in PPy-MoS_2 (pristine) composite system. An ample amount of interconnected nanosheets have been gathered together forming floating sheets in the composite system (Figure 6.5(a.3)). The free basal area of these transparent MoS_2 nanosheets suitably execute the synergic increment in electrochemical activity of the host polymer matrix. Upon irradiating 90 MeV C^{6+} ion beam of fluence 3.5×10^{11} ions/cm^2, closely arranged polymer grains can be found, as shown in Figure 6.5(b.1). The compact packing of

the polymer nanoparticles is eventually driven by the cross-linking phenomena occurring inside the polymer matrix during this moderate fluence [225]. To be mentioned, the charge transfer path length has been reduced in this cross-linked system which emphasizes the smooth carrier transport throughout the polymer chain. Also, the damage caused via energetic ion beams over the MoS_2 sheets are clearly visible in Figure 6.5(b.2). Formation of these scattered nano pores on the composite surfaces can hinder the fair diffusion of the electrolyte towards the system electrode, resulting in an augmented double layer capacitance (C_{dl}) in the electrode system. The sprinkled black batches in Figure 6.5(b.3) also confirm the formation of the small pores over the surface of the composite system.

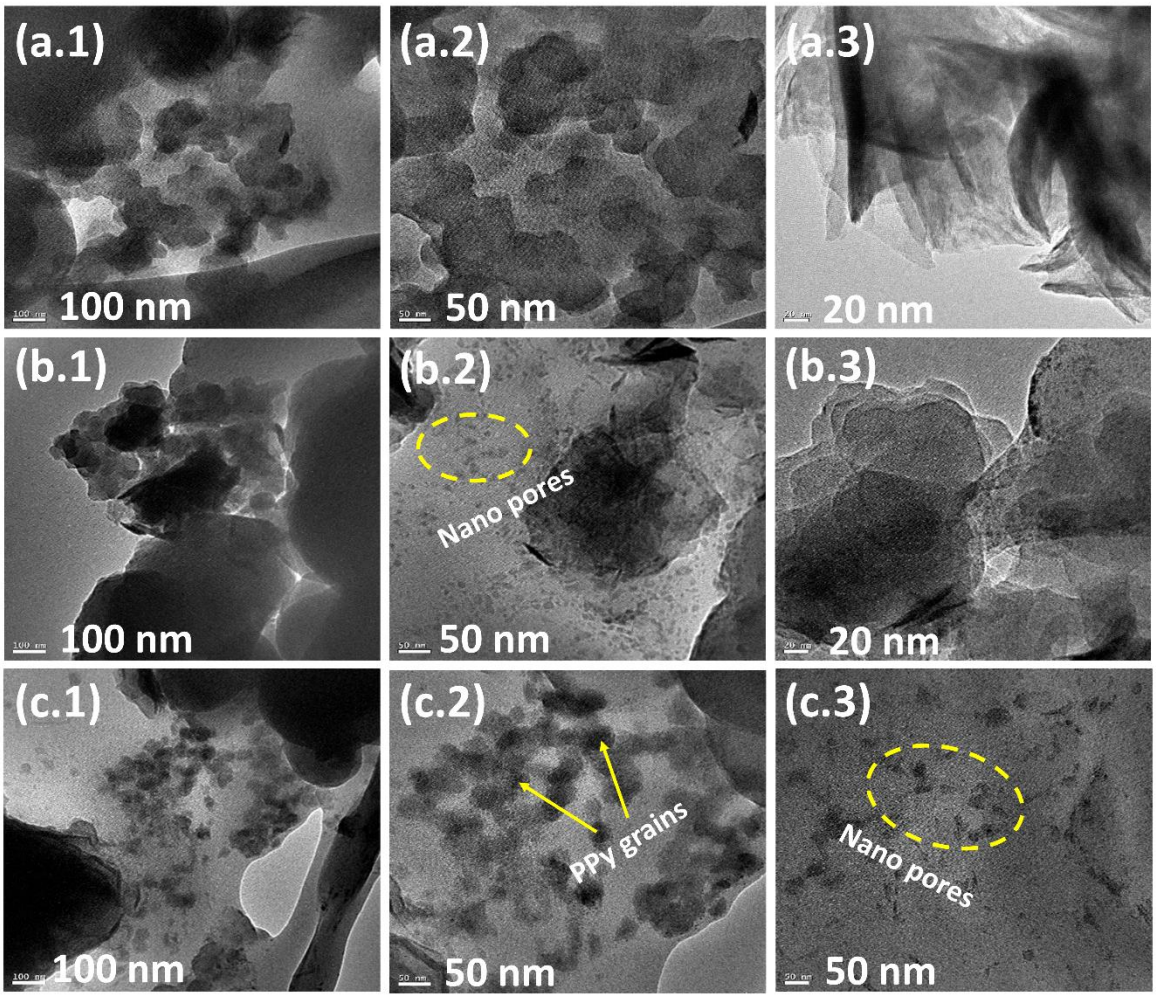

Figure 6.5: TEM micrograph of (a.1-a.3) PPy-MoS_2 (pristine), and irradiated PPy-MoS_2 composite systems at a fluence of (b.1-b.3) 3.5×10^{11} ions/cm^2, (c.1-c.3) 1.0×10^{13} ions/cm^2 and at different magnifications

Again, at the fluence of 1.0×10^{13} ions/cm^2, the sparse distribution of the polymer grains inside the MoS_2 can be observed in Figure 6.5(c.1), which substantiates the fact that disordered chain scissioning and chain breaking would take place in the polymer system at the highest fluence. At this fluence, the polypyrrole grains are partially departed from each other, further impeding the effective carrier hopping process in the polymer system and giving rise to higher charge transfer resistance (R_{ct}) at the interface of the electrolytic system. Upon increasing the fluence the diameter of the ion beam-induced nanopores have been increased. This can be realized from Figure 6.5(c.3) where the excess energy deposition through electronic energy loss originated the rapid annealing effect in the composite system causing a diminution in crystallinity and formation of denser as well as overlapped ion tracks.

6.3.4. Cyclic voltammetry (CV) study of the pristine and irradiated PPy-MoS_2 composites

The CV responses were taken at a scan rate of 20 mV/s under the potential window of -0.2 V to +0.6 V in 0.1 M PBS solution containing 5 mM $K_3[Fe(CN)_6]$ as redox probe. It can be observed from Figure 6.6(a) that the area under the CV curve increases upon incorporation of MoS_2 in the polymer system. MoS_2 being an electroactive TMDC candidate can enhance the conductivity of the host material while providing larger surface area, allowing rapid electrochemical charge transfer [226]. In this figure, the increase in redox peak height after incorporation of MoS_2 suggests superior redox activity of PPy-MoS_2 system than its bare PPy counterpart. Figure 6.6(b) depicts the CV curves corresponding to the pristine and ion beam irradiated PPy-MoS_2 systems. On comparing, one can find that the CV response of the system irradiated with the fluence of 1.0×10^{10} ions/cm^2 is nearly similar to the pristine/unirradiated one; while the response is quite decent at the fluence of 3.5×10^{11} ions/cm^2. Also, the lower peak potential separation obtained in the blue CV curve of Figure 6.6(b) indicates a better diffusion process along with a higher amount of electron transfer occurring in the system irradiated with the fluence of 3.5×10^{11} ions/cm^2. This can be due to the impact caused by the energetic ion beams in our composite system that results in the cross-linking of polymer chains at this moderate dose, facilitating smooth hopping of carrier charge through the entangled chains. But beyond this fluence, the peak height as well as the area under the CV curves will decrease, with the redox peak disappear at the highest fluence of 1.0×10^{13} ions/cm^2. The overlapped ion tracks and chain breaking led disorder which causes constraints against charge transport thus resulting in the disappearance of the redox activity of the PPy-MoS_2 composite.

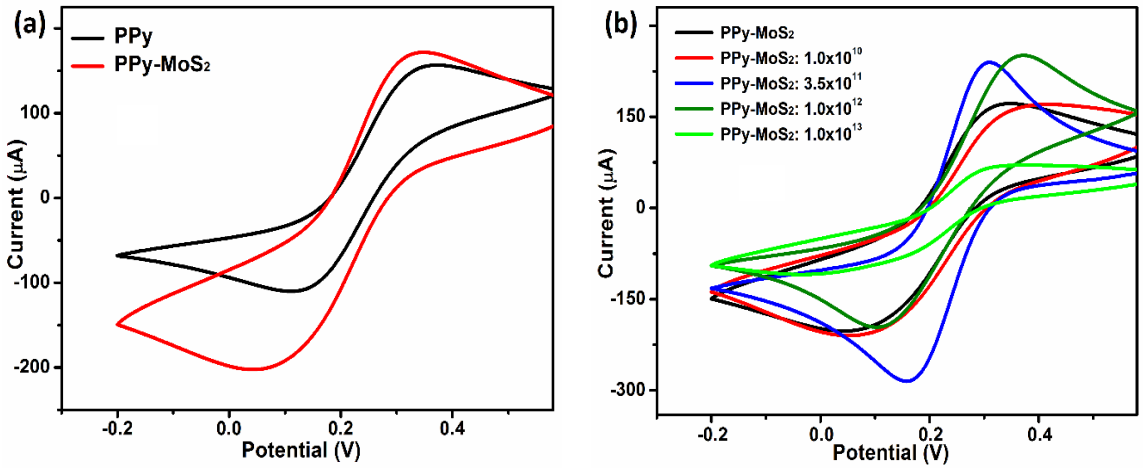

Figure 6.6: Comparison of the CV responses of (a) PPy and PPy-MoS_2 system, (b) PPy-MoS_2 (pristine) and samples irradiated with different fluences

6.3.5. Impedance spectroscopy (EIS) study of the pristine and irradiated samples

The impedance spectra of the pristine and irradiated samples were taken by varying the frequency from 0.1 Hz to 1 MHz in 0.1 M PBS solution consisting 5 mM $K_3[Fe(CN)_6]$ as redox agent. In Figure 6.7(a) and (b), the dotted curves represent the experimentally obtained spectra, whereas the continuous lines represent the fitted spectra. To evaluate the complex interfacial impedance parameters, the inset Randle equivalent circuit is used for fitting these spectra. The meaning and significance of each parameter in the equivalent circuit have been outlined in section 2.3.6 of Chapter 2. In Figure 6.7(a), the value of R_{ct} decreases from 2.38 kΩ to 2.07 kΩ after insertion of MoS_2 in the polymer system indicating a better electron transport mechanism taking place at the interface of the PPy-MoS_2 system as compared to its PPy counterpart. In Figure 6.7(b), the fitting of the EIS spectra for pristine and irradiated systems were performed by using the Randle circuit of Figure 6.7(a). But a different equivalent circuit (depicted in the inset circuit of Figure 6.7(b)) has been used to fit the Nyquist plot corresponding to the system irradiated with $3.5x10^{11}$ ions/cm^2 fluence or MPy:2 system. In the inset circuit of Figure 6.7(b), R_3 is another resistance called solid electrolyte interface (SEI) resistance that might have appeared due to the multifaceted interfacial contact between the surface modified composite system and the electrolyte.

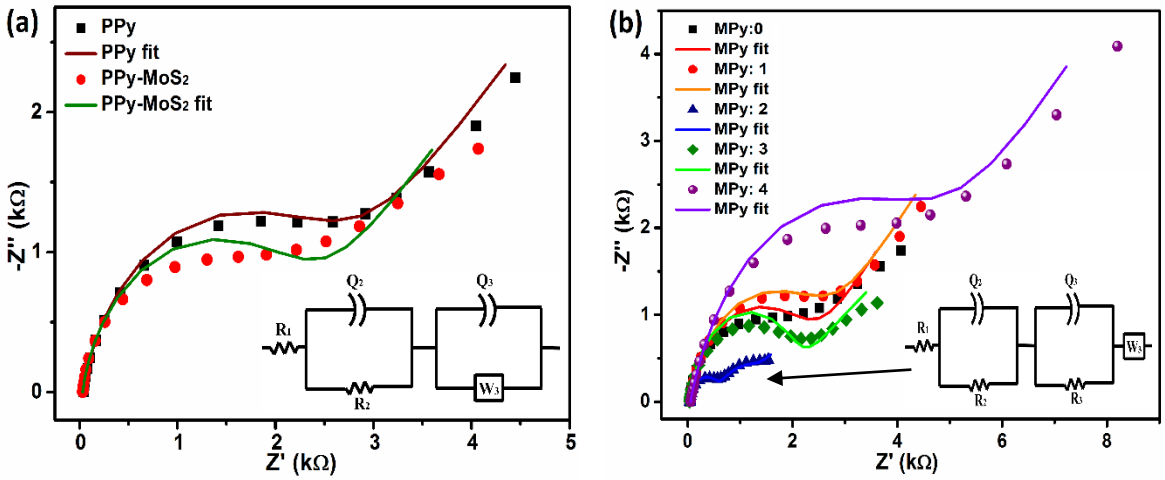

Figure 6.7: Comparison of the EIS spectra of (a) PPy, and PPy-MoS_2 composite system, (b) PPy-MoS_2 (pristine) and irradiated samples

The fitted parameters of the pristine and irradiated samples are mentioned below in Table 6.1. On comparing the R_2 values, we can observe that the magnitude of R_{ct} in case of MPy:1 system is almost comparable to the pristine one and it is the lowest (0.49 kΩ) in case of MPy:2 system. But this interfacial impedance value has become maximum at the highest fluence of $1.0x10^{13}$ ions/cm^2. Similarly, the Q_2 or C_{dl} value decreases drastically as one moves from pristine system to the irradiated one with fluence $3.5x10^{11}$ ions/cm^2. Whereas, in the case of MPy:3 system, the C_{dl} value didn't differ much from the MPy:2 one and at 1.0×10^{13} ions/cm^2 fluence the value rises to 12.06 µF. On analyzing the R_{ct} and C_{dl} values of pristine and irradiated systems, one can say that at the lowest fluence of 1.0×10^{10} ions/cm^2, the disordered polymer chains would restrict the smooth transport of carrier via hopping mechanism resulting in an augmented R_{ct} value. Also, the interaction of energetic C^{6+} ions contributed to the surface modification of the composite system towards the formation of small latent tracks over the MoS_2 incorporated polymer system. This radiation induced pores hinder the effective diffusion of ions and radicals towards the surface of the electrode causing poor coulombic interaction in between the working electrode and counter ions/radicals of the electrolyte giving rise to a drop in the C_{dl} value. As discussed earlier, the cross-linking and restacking of the polymer chains took place upon increasing the fluence to 3.5×10^{11} ions/cm^2, so at this flux rate the interfacial charge transport becomes efficient with a lower R_{ct} value of 0.49 kΩ. In addition, the C_{dl} value further decreased to 8.06 µF against the flux of 1.0×10^{12} ions/cm^2. This decrease in the C_{dl} value indicates the formation of adequate nanopores over the PPy-MoS_2 surface that further

causes a drop in the coulombic interaction by lessening the double layer region. Nevertheless, at the maximum fluence of 1.0×10^{13} ions/cm^2, the overlapping of the latent tracks took place in the MPy:4 system causing excess breakage of the polymer backbones and wider irradiation track formation which can also be confirmed from the TEM micrograph image of Figure 6.5(c.3). Again, this wide scratch or latent track facilitates a well diffusion of the ions/radicals towards the surface causing a hike in the C_{dl} value to 12.06 µF. Now, on comparing the Q_3 values of all the systems, one can find that this CPE parameter almost remains uniform in all the cases. But it drastically increases for MPy:2 system due to the formation of additional SEI layer which might have emerged due to the interaction of radiation induced multifaceted polymer grains with the MoS_2 sheet causing larger interfacial contact regime. Finally, the value of Warburg impedance (W_3) also changes depending upon the ion flux. As can be viewed from Table 6.1, W_3 value is maximum in case of MPy:2 system, while it is minimum for the highest fluence that might be due to the smooth diffusion of the carrier ions into the wider latent tracks generated at the of highest fluence.

Table 6.1: EIS derived parameters of the pristine and irradiated samples

Electrodes	R_1 (Ω)	R_2 (kΩ)	Q_2 (µF) η	Q_3 (µF) η	W_3 (×10^{-6}) S.$s^{1/2}$	
PPy	40.28	2.38	55.18 η=0.99	24.13 η=0.87	392.01	
PPy-MoS_2: no fluence ions/cm^2 (MPy:0)	33.14	2.07	52.18 η=1.00	23.53 η=0.88	532.70	
PPy-MoS_2: 1.0×10^{10} ions/cm^2 (MPy:1)	40.45	2.18	25.95 η=1.00	24.57 η=0.88	385.92	
PPy-MoS_2: 3.5×10^{11} ions/cm^2 (MPy:2)	43.05	0.49	9.52 η=0.96	387.10 η=0.80	R_3 (kΩ)	W_3 (x10^{-6})
					0.64	827.14
PPy-MoS_2: 1.0×10^{12} ions/cm^2 (MPy:3)	33.99	1.812	8.06 η=0.04	8.36 η=0.98	566.26	
PPy-MoS_2: 1.0×10^{13} ions/cm^2 (MPy:4)	56.80	3.75	12.06 η=0.94	23.23 η=0.88	243.17	

6.3.6. Determination of electrochemical parameter of pristine and the irradiated PPy-MoS_2 composites

To compare the electrochemical behavior of the pristine and irradiated systems, modified Randle-Sevcik equation was used to evaluate the redox active area of all the electrode systems. This equation basically provides a linear relation between peak current (i_p) and sq. root of scan rate ($\upsilon^{1/2}$), as follows: $i_p = 2.69 \times 10^5 \times n^{3/2} A D^{1/2} \alpha^{1/2} C \upsilon^{1/2}$ (at T=300 K). The parameters have their usual meanings as stated in section 3.3.3 (Equation 3.1). The value of *A* can be easily estimated from the slope (ζ) of the i_p vs $\upsilon^{1/2}$ plot, as: $A = \frac{\zeta}{2.69\times10^5\times n^{3/2} C \alpha^{1/2} D^{1/2}}$. As shown in Figure 6.8(a-e), the CV responses of pristine and irradiated samples were taken by varying the scan rate from 30-150 mV/s under the potential range of -0.2 V to +0.6 V in PBS solution comprising of 5mM $[Fe(CN)_6]^{3-/4-}$ as redox agent. In the inset graph of Figure 6.8(a-e), the peak oxidation current (i_{pa}) w.r.t. $\sqrt{\text{scan rate}}$ ($\upsilon^{1/2}$) of the respective CV cycles has been plotted by linear fitting the obtained data points. In each set of CV responses, it could be observed that i_{pa} is varying linearly w.r.t. $\sqrt{\text{scan rate}}$, indicating a diffusion-controlled process taking place in all the systems. Apart from this, the peak potential separation (ΔE_p) is higher than 59 mV in the CV responses indicating non reversible redox process taking place in the systems. For a non-reversible redox process, the peak current (I_p) depends upon the reaction rate (k_s) as follows,

$$ln(I_p) = ln(0.227FAk_sC) - \frac{\alpha F}{RT}(E_p - E_o) \qquad (6.1)$$

The above relation has already been referred in Equation 3.3. Here, the formal potential E_o is the intercept of linearly fitted E_p vs (scan rate) plot of Figure 6.9(a.1-e.1). The value of α and k_s have been evaluated from the $ln(i_{pa})$ vs $(E_p\text{-}E_o)$ plot of Figure 6.9(a.2-e.2). The obtained values of electroactive area, transfer coefficient and reaction rate associated with all the system electrodes can be found from Table 6.2. The creation of surface defects at low dose of 1.0×10^{10} ions/cm^2 fluence eventually hamper the interfacial contact of electrode and electrolyte causing a little drop in the value of *A*. While a moderate fluence of 3.5×10^{11} ions/cm^2 has proved to be suitable for our MoS_2 incorporated conducting polymer-based electrode system for better electrochemical performance. This is because, the cross-linking of polymer chains is expected to take place at this flux rate providing a better pathway for carrier movement via π-delocalization. Also, probing of MoS_2 sheets and creation of columnar defects can help in

superior electrical contact in between layered MoS_2 and polymer matrix which further diminishes the junction resistance, resulting in an augmented electrochemical conductivity. Moreover, the high fluences of 1.0×10^{12} and 1.0×10^{13} ions/cm^2 could generate excess defects as well as chain scissioning that constraints the π-delocalization mechanism and minimizes the redox efficiency [227]. Hence, a lesser electroactive area has been attained over the highest fluence.

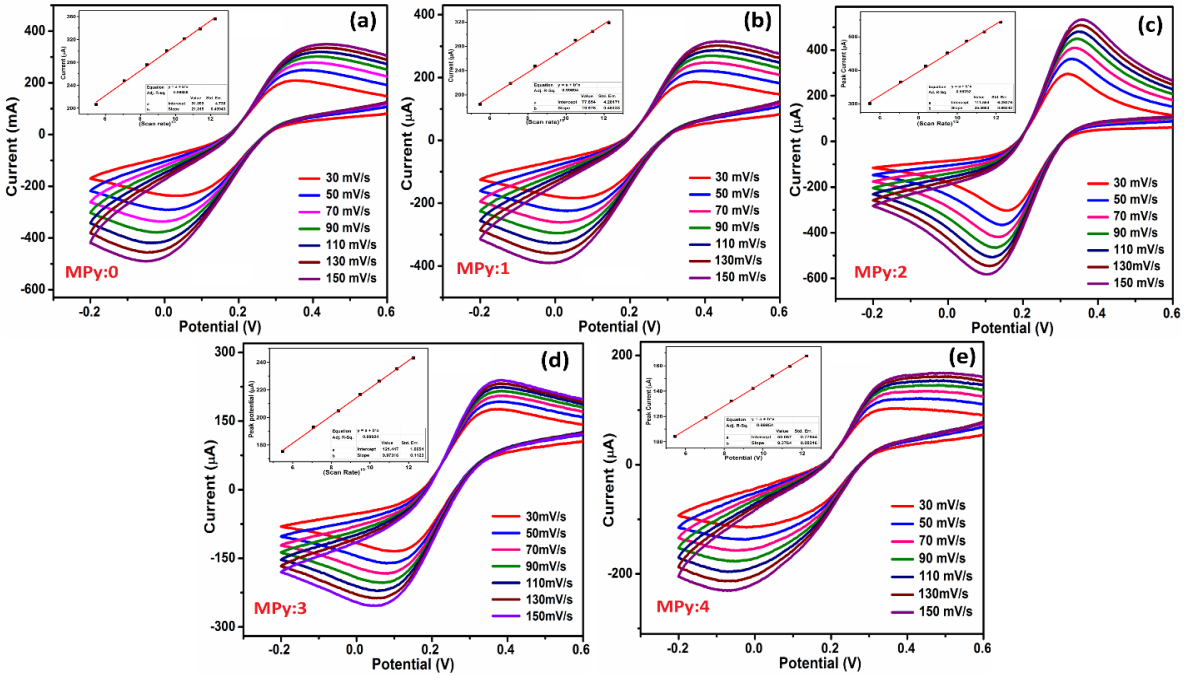

Figure 6.8: Scan rate variation plot with inset i_p vs $v^{1/2}$ graph of PPy-MoS_2 nano-composite system, (a) without (pristine), and with irradiation at a fluence of (b) 1.0×10^{10}, (c) 3.5×10^{10}, (d) 1.0×10^{12}, and (e) 1.0×10^{13} ions/cm^2

From the above discussion, it could be noticed that, 90 MeV C^{6+} ion beam of flux density 3.5×10^{11} ions/cm^2 has conveyed a constructive impact in our PPy-MoS_2 derived composite system. The controlled defect creation and material modification cause the enhancement in electrochemical properties at this moderate ion dose. In a similar way, the values of k_s are in the order of 1×10^{-5} s^{-1} which indicate electrochemical irreversibility of all the electrodes. Table 6.2 depicts that the rate of the redox process increases noticeably at the moderate fluence of 3.5×10^{11} ions/cm^2 and above. Formation of accessible pores at higher fluences allow smooth diffusion of the electrolyte over the electrode, providing an improved kinetics with fast charge transport towards the specific electroactive area.

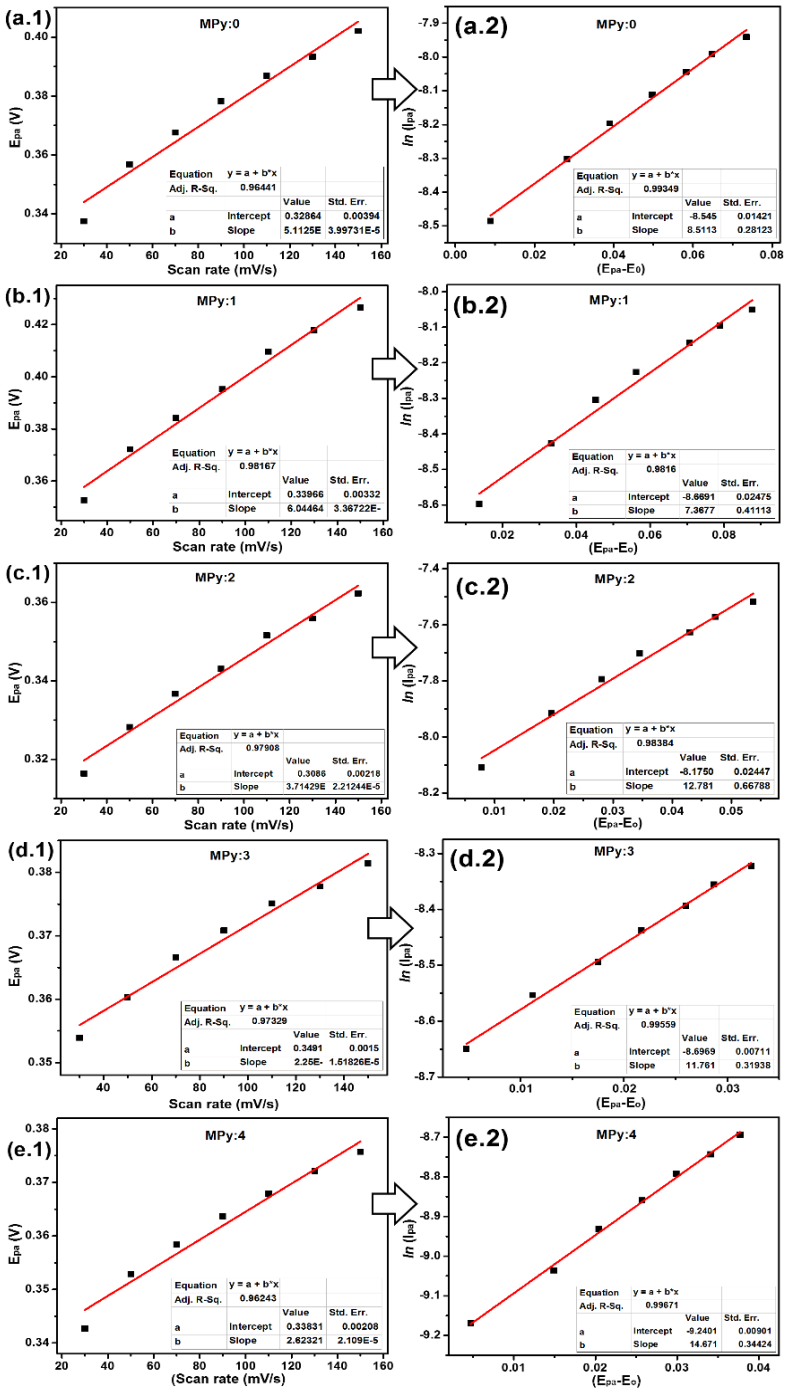

Figure 6.9: E_{pa} *vs* (scan rate) plot of PPy-MoS_2 composite system (a.1) without irradiation and irradiated with fluence of (b.1) 1.0×10^{10}, (c.1) 3.5×10^{11}, (d.1) 1.0×10^{12}, (e.1) 1.0×10^{13}, ions/cm^2 and, *ln* (I_{pa}) *vs* (E_{pa}-E_o), plot of PPy-MoS_2 composite system (a.2) without irradiation and irradiated with fluence of (b.2) 1.0×10^{10}, (c.2) 3.5×10^{11}, (d.2) 1.0×10^{12}, and (e.2) 1.0×10^{13}, ions/cm^2

On the other hand, it can be observed in Table 6.2 that the value of *A* decreases drastically for MPy:3 and MPy:4 composites due to the excess defect caused by annealing, which typically generates more amorphous regions consisting of disordered polymer chains along with the MoS_2 sheets wrecked by excessively high dose of ion beam. This results in the diminution of redox active sites that can be expected from the lower value of *A* in case of use of higher ion fluences. Whereas, the ion track formed during these fluences can improved the electrolytic contact of the electrodes offering a higher value of rate constant corresponding to the higher fluences.

Table 6.2: Electroactive area corresponding to pristine and irradiated systems

Electrode Type	**Electroactive Area (cm^2)**	**Transfer coefficient (α)**	**Rate constant (k_s) ($\times 10^{-5}$ s^{-1})**
MPy:0	0.3509	0.22	0.502
MPy:1	0.3459	0.19	0.453
MPy:2	0.4485	0.36	0.573
MPy:3	0.1331	0.31	1.140
MPy:4	0.1149	0.37	0.767

6.3.7. Detection of Goat anti-mouse *IgG* by differential pulse voltammetry (DPV) technique

After monitoring the electrochemical performance of the pristine and irradiated electrode systems, determination of sensing activity was considered for the as fabricated immunosensor probes. As for fabrication of the immunosensors, mouse *IgG* antibody was immobilized over the surface of the pristine and irradiated electrodes via glutaraldehyde cross-linking method followed by blocking of the non-specific sites by using BSA. Afterwards, the as prepared biosensor probes were utilized for the detection of the specific antigen (Goat anti-mouse *IgG*) by electrochemical means. Figure 6.10(a-e) illustrate the DPV responses of the pristine and irradiated immunosensors in presence of different concentrations of the antigen in the solution. Herein, the DPV spectra were taken under the potential range of -0.2 V to +0.6 V in 0.1 M PBS solution containing 5 mM $[Fe(CN)_6]^{3-/4-}$ as a redox probe. In each figure below, the black spectrum represents the DPV response of the sensor in absence of the antigen in the solution.

Later on, the DPV responses were acquired by varying the concentration of goat anti-mouse *IgG* from 5-290 ng/mL in the PBS solution. It can be observed that the DPV current declines upon increasing the concentration of the antigen as shown in Figure 6.10(a-e). To be mentioned, the biomolecules are very selective to their specific antigen only and they bind with each other upon close proximity giving rise to a dielectric antibody-antigen (*Ab-An*) abduct layer. So, when the surface immobilized antibody binds with the antigen in the solution via physisorption then thickness of the dielectric layer increases at the solid-electrolyte boundary which further impedes the interfacial charge transfer process [228]. As a result, lower DPV current has been experienced after every injection of antigen in the solution (Figure 6.10(a-e)). The proportional drop in current upon subsequent addition of antigen has led to the noticeable change in current (ΔI) vs concentration of antigen ([C]) plot, as shown in the left side inset graphs of Figure 6.10(a-e). From the ΔI vs [C] plot, it has been observed that the data points exhibited a decent fit when they are fitted by using Langmuir adsorption isotherm equation, given as: $I = \frac{I_0}{1+\frac{B}{[C]}}$; where, I_o represents saturated current response and B is the inverse of Langmuir adsorption coefficient (k). The adsorption isotherm proposed by Langmuir is a single layer surface adsorption mechanism which is commonly used to describe the equilibrium in between adsorbate and adsorbent system. The right-side adjacent images of Figure 6.10(a-e), showing the $1/\Delta I$ vs $1/[C]$ plots for the respective pristine and irradiated immunosensor probes. The linear behavior of this plot confirms that the adsorption mechanism taking place in our fabricated sensor is Langmuir type. Again, this plot also helps in determining the sensing parameters like limit of detection (*LOD*) and sensitivity of the immunosensor. Basically, from the slope of the linear plots of Figure 6.10, we can obtain the $(LOD)^{-1}$ value by using the relation; $\frac{3.3\times\sigma_y}{m}$, where, σ_y is the standard error of y-intercept and m is the slope of the calibrated straight line. Finally, the *LOD* can be calculated by taking the inverse of already estimated $(LOD)^{-1}$ value. The obtained values of detection limit and sensitivity corresponding to both pristine and irradiated immunosensors have been tabulated in Table 6.3. As can be seen in the table, a low *LOD* value of 30.42 ng/mL or 0.203 nM with a comparatively high sensitivity magnitude of 10.00 μA $ng^{-1}mL\ cm^{-2}$ can be achieved by modifying the electrode using 90 MeV C^{6+} ion irradiation at a fluence of 3.5×10^{11} ions/cm^2.

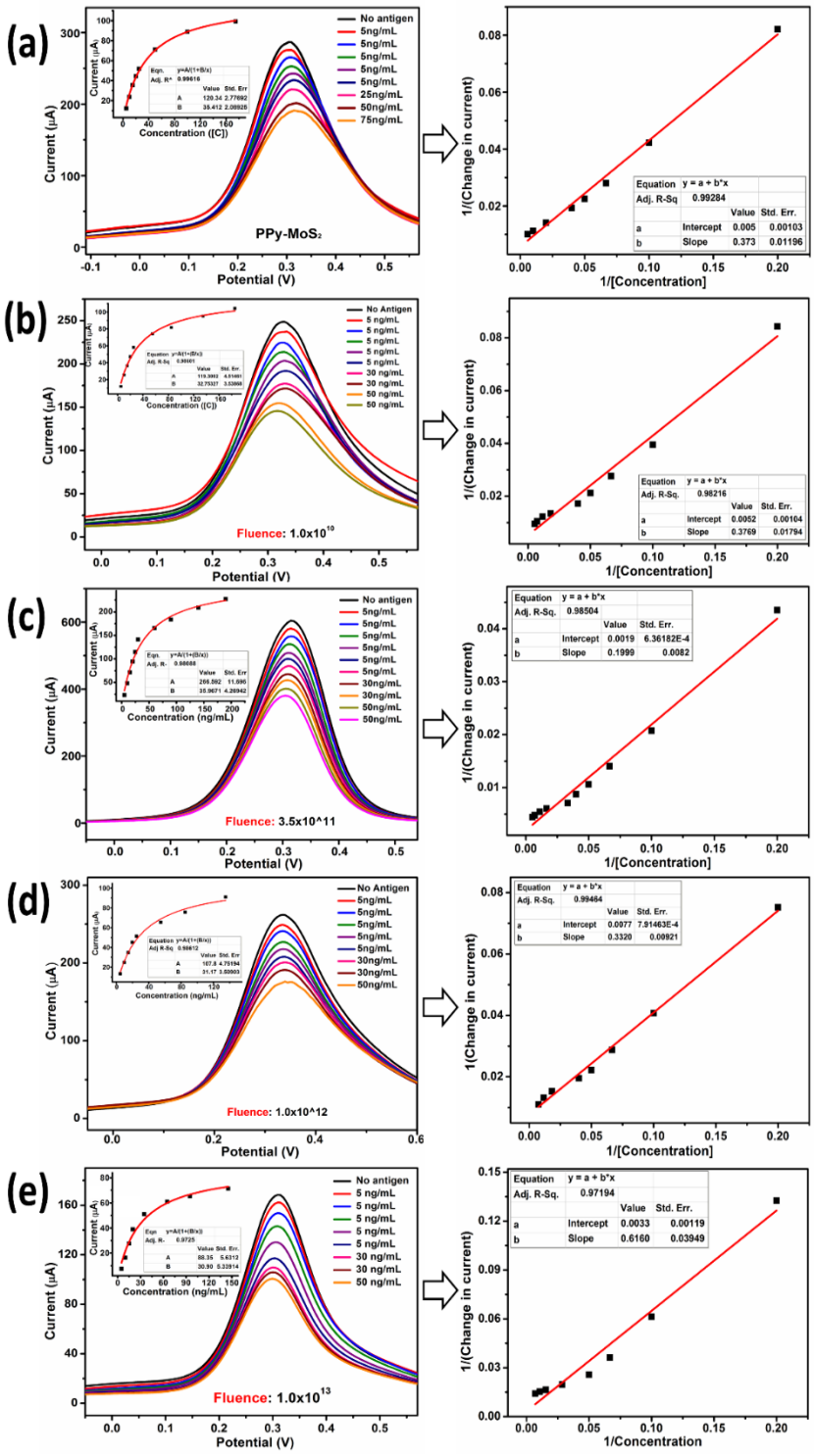

Figure 6.10: DPV response, ΔI vs $[C]$ plot and $1/\Delta I$ vs $1/[C]$ plot of PPy-MoS_2 composite system (a) without irradiation and irradiated with fluence of (b) 1.0×10^{10}, (c) 3.5×10^{11}, (d) 1.0×10^{12}, and (e) 1.0×10^{13} ions/cm^2.

Table 6.3: *LOD* and sensitivity values of irradiated systems

Immunosensor systems	*LOD* (ng/mL)	Sensitivity (μA mL ng^{-1} cm^{-2})
MPy:0	38.74	5.306
MPy:1	36.60	5.236
MPy:2	30.42	10.000
MPy:3	45.02	6.024
MPy:4	55.45	3.246

6.3.8. Discussion on the sensing of immunosensor based on PPy-MoS_2 nanocomposite

The detection mechanism of the immunosensor probe modified with 3.5×10^{11} ions/cm^2 fluence is further discussed in this section. Figure 6.11(a) and (b) depicts, respectively the CV and EIS responses monitored after each process step during the sensor fabrication and sensing experiment. The black curve of Figure 6.11(a) represents the CV response of the MPy:2 system where the sharp redox peaks appearing at +0.31 V and +0.16 V are due to the oxidation and reduction of $[Fe(CN)_6]^{3-/4}$ present in the PBS solution, respectively. Similarly, in Figure 6.11(b), the black spectrum resembles the Nyquist plot for the MPy:2 system. In this plot, the diameter of the small suppressed semicircle gives the R_{ct} value of the system at the electrode-electrolyte interface. On analyzing both the figures, it can be observed that the peak height along with the area under the CV curves decreases and the R_{ct} value in the impedance spectra increases after glutaraldehyde treatment (red curve) and immobilization of the mouse *IgG* antibody (blue curve) over the MPy:2 electrode system. The reactive glutaraldehyde molecules bind with the functional moieties and polar segments of the ion beam modified PPy-MoS_2 system followed by covalent linkage formation with the -NH_2 group of the antibody. Basically, the fabrication of immunosensor involves immobilization of the antibody over the electrode *via* formation of covalent-linkage which eventually set up additional layers over the electrode surface that hamper the interfacial charge transfer during the redox process. The decrease in peak height in the CV responses and the increase in R_{ct} value in impedance spectra indicates successful fabrication of the immunosensor via requisite immobilization of the mouse *IgG* antibody over the MPy:2 substrate.

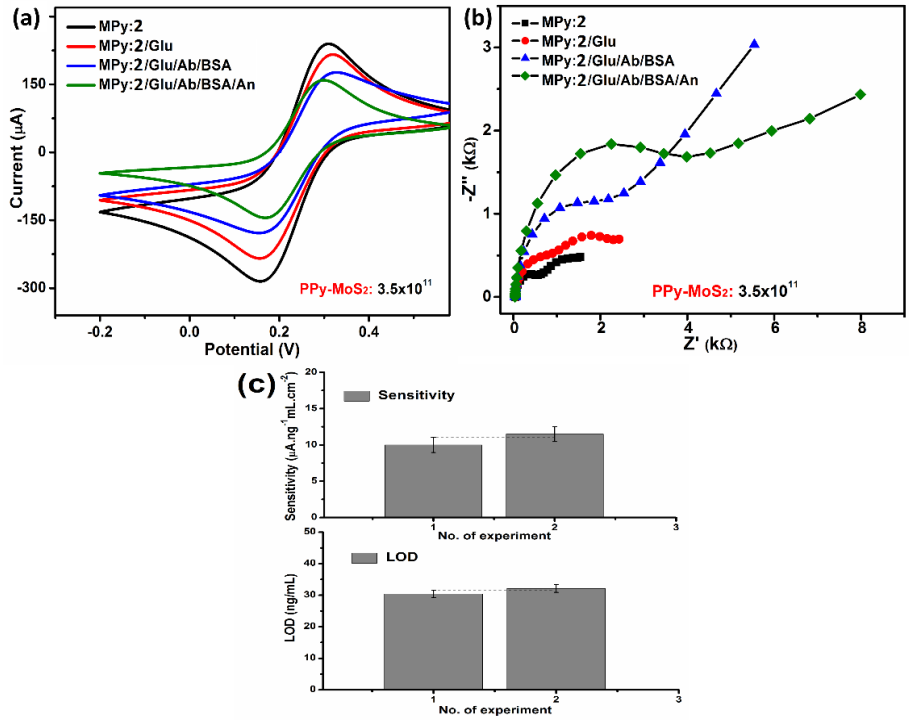

Figure 6.11: (a) CV and (b) EIS responses of the MPy:2 system monitored throughout the sensor fabrication and sensing experiment, (c) repeatability test for the MPy:2 system.

Afterwards, due to added specific antigen (Goat- anti mouse *IgG*) in the solution, it selectively got attached with the mouse *IgG* over the immunosensor. The antibody-antigen abduct behaves as an additional dielectric layer over the sensor electrode, which again hindering the effective electron transfer at the solid-electrolyte boundary. In Figure 6.11(a) and (b), the further decrease in the CV area and increase in R_{ct} value of the EIS response (green spectrum) taken after antigen injection confirms the occurrence of antibody-antigen interaction in our system. The repeatability aspect was checked by repeating the sensing experiment in case of MPy:2 system, in which we have experienced better sensing activity. The DPV response along with the inset ΔI *vs* $[C]$ and $^{1}/_{\Delta I}$ *vs* $^{1}/_{[C]}$ plots are shown in Figure 6.12(a) and (b), respectively. The obtained values of *LOD* and sensitivity from both the repetitive experiments are represented as histograms in Figure 6.11(c). Here, the overlapped error bars in both the plots suggests that the values of *LOD* and sensitivity estimated from the repetitive experiments are quite indifferent from each other.

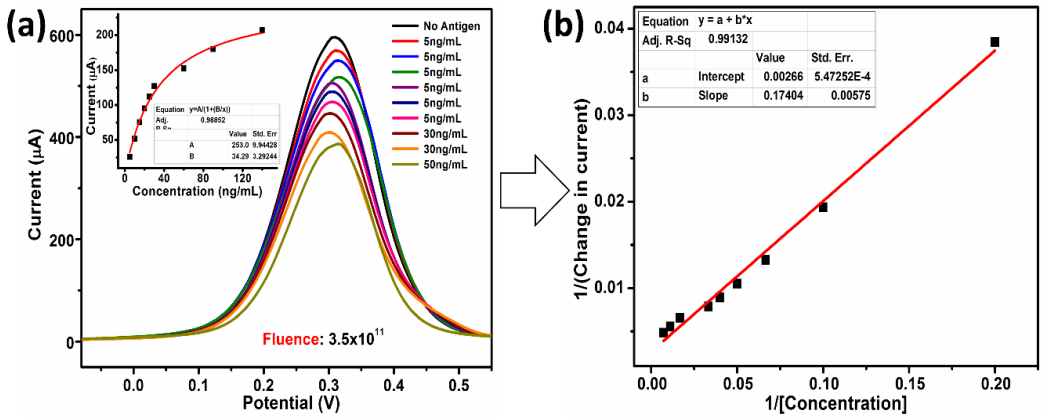

Figure 6.12: (a) DPV response with inset ΔI vs [C] plot, and corresponding (b) $1/\Delta I$ vs $1/[C]$ plot, for MPy:2 system

6.4. Conclusions

The present study describes a strategy for electrochemical sensing after material modification caused by high energy ion beam irradiation. Analytical studies illustrate the fluence dependent tuning of the electrochemical as well as other spectroscopic behavior of PPy-MoS_2 nanocomposite. Interestingly, maximum cross-linking in the polymer matrix was found at a certain fluence contributing to high catalytic amplification. Further, this ion beam modified system was subjected to immunoassay assessment for the detection of goat anti-mouse *IgG*. Significant enhancement in the sensing parameters of the irradiated system highlights the potential applicability of the ion beam based material modifications. The fabricated immunosensor executed selective detection of the target analyte with a low *LOD* of 0.203 nM and high sensitivity value of 10.0 $\mu AmLng^{-1}\ cm^{-2}$ under a wide detection range. The attractive feature of this research is the effect of ion irradiation for reshaping the electrochemical as well as spectroscopic behavior of the PPy-MoS_2-derived electrocatalyst toward its potential application as a high-performance electrochemical immunosensor. Future works may be envisioned to transform the immunoassay technique into a chip-based assay for point of care (POC) clinical diagnosis.